Evaluation of Density Fields of Numerical Analysis Output of Solid Carbon Dioxide Extrusion Process

Jan Górecki[1*], Tymoteusz Lindner[1], Krzysztof Wałęsa[1]

[1] Faculty of Mechanical Engineering, Poznan University of Technology, ul. Piotrowo 3, 60-965 Poznan, Poland
* Corresponding author's e-mail: jan.gorecki@put.poznan.pl

ABSTRACT

Efforts to reduce energy consumption and explore alternative energy sources are paramount in production process research. However, a research gap exists regarding the evaluation of density fields in numerical analysis output of solid carbon dioxide (CO_2) extrusion. This study aims to address this gap by examining the density fields in the numerical analysis output of the extrusion process for solid CO_2, commonly known as dry ice. Dry ice, a by-product of ammonia compounds production, requires efficient management due to its high sublimation rate. Ram pressing is a commonly used method for compressing dry ice, but the resulting product often exhibits non-uniform density fields, presenting challenges for process optimization. To bridge this research gap, an algorithm is verified for determining the percentage share of density fields in the numerical simulation results. By comparing simulations using single- and multiple-cavity dies, the algorithm provides valuable insights into the distribution of density within the extruded solid CO_2. In overcoming the limitations of subjective comparative evaluation, this study offers objective measures for assessing and comparing numerical analysis outputs. The findings contribute to a deeper understanding and optimization of the solid CO_2 extrusion process, facilitating the production of high-density dry ice products with reduced energy consumption. In conclusion, this research not only bridges the research gap in evaluating density fields but also advances the field of solid CO_2 extrusion and waste materials management.

Keywords: FEM; image analysis; CO_2; dry ice; extrusion; compaction.

INTRODUCTION

One of the topical issues in the area of production process research and development efforts are the methods allowing reduction of energy input of the process [1, 2] and new alternative sources of energy [3, 4]. These efforts are triggered by limited availability of energy resources [5] and increasing energy prices [6]. Tahmasebi et al. 2011 pointed out that less energy consumption in production translates to lower carbon footprint of the end-product [7].

Also, a literature review shows efficient solutions in the area of waste materials management [8]. Management of biodegradable materials is based on two principal technologies: composting [9] and densification to solid fuel [10], if and as appropriate. In the latter case, reduction of energy consumption is ever more important [11] due to involvement of energy intensive processes of compression [12, 13] and extrusion [14].

Carbon dioxide is an example of such waste materials. Bicer et al. 2017 pointed that carbon dioxide is generated in large quantities as a by-product of ammonia compounds production process [15]. In order to facilitate its management, it is liquefied through compression to over 20 bar [16]. During subsequent expansion, a part of the material turns into crystals. The sublimation point of solid carbon dioxide is -78.5 °C [17], i.e. it sublimates in normal ambient conditions. These two above-mentioned properties resulted in it being referred to by the common name "dry ice" (DI).

Dry ice has many applications, including surface cleaning [18, 19] and conveying of products at low temperatures [20]. However, for efficient use, DI must be densified to reduce sublimation rate [21].

Ram pressing is most commonly used DI compression method. Berdychowski et al. 2022 described all the stages of the dry ice production process in the machine whose working system is shown schematically in Figure. 2 [22].

The dry ice extrusion process comprises compression and extrusion stages [23]. The available literature includes reports of numerical simulation studies of this process [24]. It is worth noting at this point that as it was demonstrated by Wałęsa et al. 2023 and Berdychowski et al. 2022 the DI compression stress and density fields vary along the Z axis of the compression cavity and the product of this process is not homogenous in terms of density over the cross-section area [24, 25].

Note that for evaluation and comparison of the numerical analyses outputs it is necessary to have access to the input data bases containing density, stress and strain values. Unfortunately, simulation output are usually presented in colour charts, with the different colours representing specific ranges of values. Thus we are limited to subjective comparative evaluation of the respective areas sizes.

This article presents the output of verification of algorithm determining the percentage share of the fields representing the simulation results. The reference value was the output of numerical simulations of the DI extrusion process through single- and multiple-cavity dies respectively.

METHODS AND MATERIALS

Materials

Both single- and multiple-cavity dies were used in the numerical studies. In single-cavity dies two parts can be identified: converging section (CS) and cylindrical barrel section. The design of converging cone cavity is shown in Figure 2.

The literature gives information on the influence of the convergent section geometry on the magnitude of forces or stress during extrusion of the material. Ternan et al. 2005, also pointed out that the shape of the convergent section sides may influence also the uniformity of the end-product density [26]. Hence, in this research numerical simulations were carried out for single-cavity dies with three different convergent section geometries, i.e. conical (CS), convex (WP) and concave/ convex (WKWP), as shown in Figure 3.
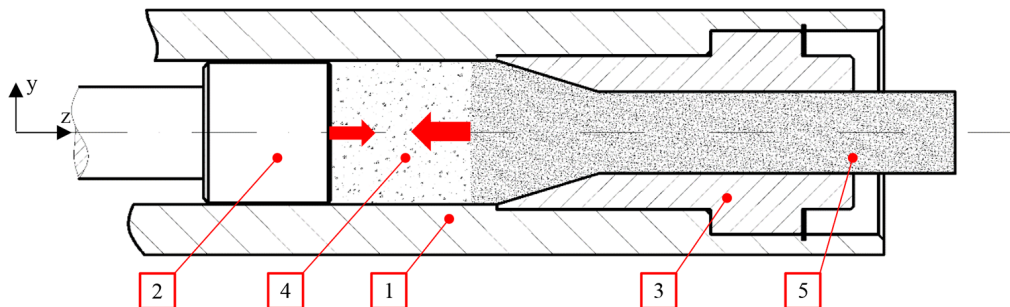

Fig. 1. Main parts of ram extruder: 1 – compression cavity, 2 – ram, 3 – single-cavity die, 4 – loose dry ice, 5 – compressed dry ice [22]
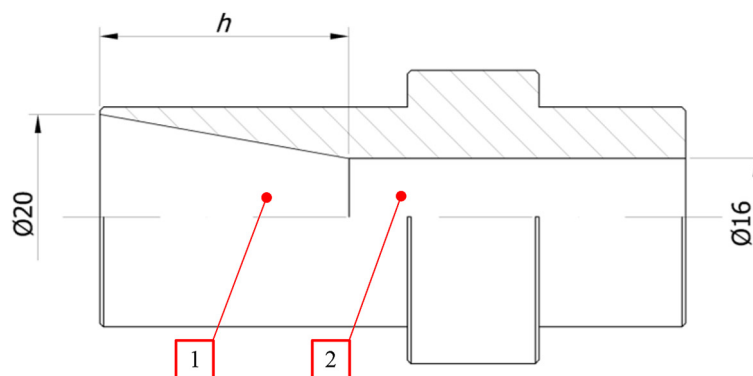

Fig. 2. Extrusion cavity of single-cavity extrusion die: 1 – convergent section; 2 – cylindrical barrel section; h – convergent section length
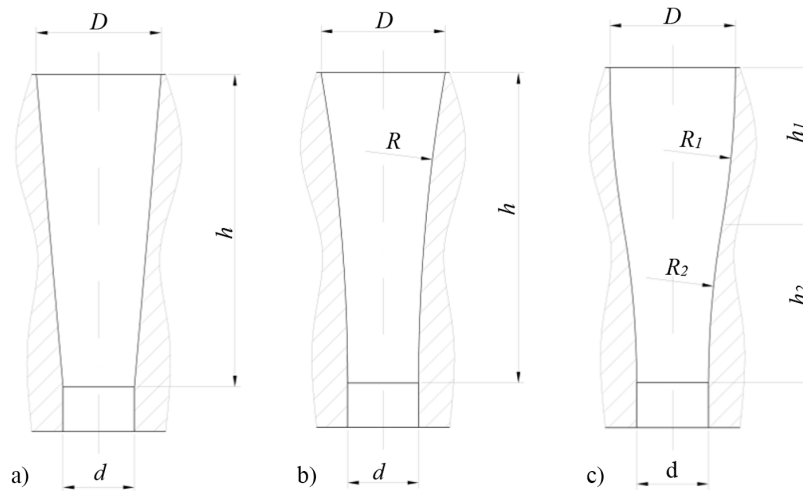
Fig. 3. Shapes of convergent sections in single-cavity die numerical simulation (a) conical section (CS); (b) concave section (WP); (c) concave/convex section (WKWP)

Biszczanik et al. 2023 [27] demonstrated that the final pellet density (ρ) depends on the convergent section length h, and thus this parameter was varied in the study, as per the following tables giving the geometrical characteristics of all the dies used in the simulations (Table 1-3)

The above defined single-cavity dies feature a circularly symmetric convergent section. This allows us to assume almost full consistency the field values distribution and their percentage share for any cross-section plane rotation angle

Table 1. Geometrical characteristics of CS single-cavity dies used in numerical simulation of dry ice extrusion process, α – section convergence angle

Type	D [mm]	d [mm]	h [mm]	α [deg]
CS	20	16	33.16	3
			22.86	5
			16.29	7

Table 2. Geometrical characteristics of WP single-cavity dies used in numerical simulation of dry ice extrusion process

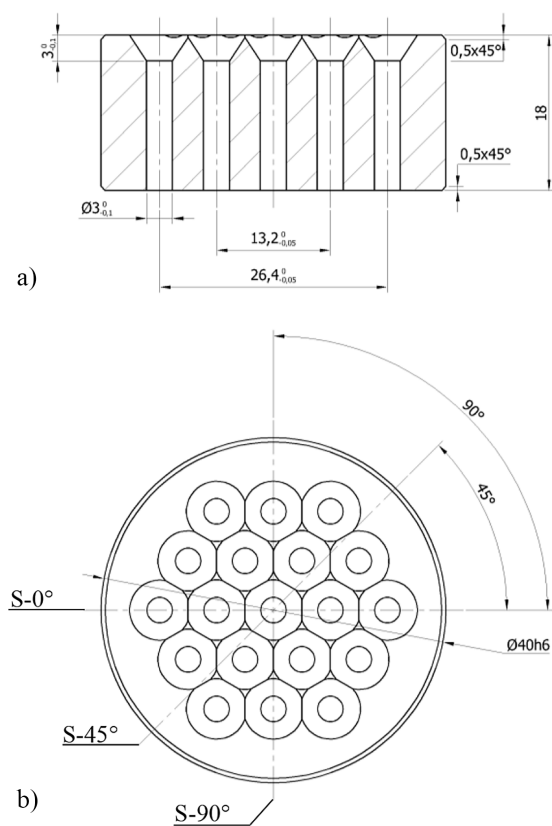| Type	D [mm]	d [mm]	h [mm]	R [mm]
WP	20	16	30	226
			40	401
			50	626

Fig. 4. Geometrical characteristics of multiple-cavity die used in the numerical simulations: (a) cross-section showing geometrical characteristics of die cavities; (b) top view showing cavity layout and location of S-0°, S-45° and S-90° planes

Table 3. Geometrical characteristics of WKWP single-cavity dies used in numerical simulation of dry ice extrusion process

Type	D [mm]	d [mm]	h_1 [mm]	R_1 [mm]	h_2 [mm]	R_2 [mm]
WKWP	20	16	15	113	15	113
			20	200.5	20	200.5
			25	313	25	313

about Z axis (Fig. 1). A different situation will be observed when analysing the results related to multiple-cavity dies. In order to investigate the differences in the percentage shares of the respective density fields a simulation of die extrusion process, as illustrated in the picture below, was carried out. In addition to the basic geometrical characteristics, the following three planes are marked in the drawing, in which the numerical analysis results are illustrated: S-0°, S-45° and S-90°.

Algorithm for analysing the percentage share of colours

Computer raster images represented in a specific colour space such as RGB, HSV [28] are made up of pixels with numerical colour codes. In 8-bit colour spaces, each pixel is represented by a number in the 0-255 range. In RGB colour space an image is represented by a 3D matrix of the following size: (image height, image width, number of die cavities). The respective cavities are, in turn, represented by a D matrix (image height and image width) representing a given colour: R – red, G – green, B – blue. Having determined the colour of a given pixel, it is possible to ascribe it to an appropriate ρ range.

The key role of the developed algorithm was to determine the percentage share of pixels of a specific colour value. The applicability of the pixel by pixel (*PbP*) method was excluded right from the start due to the long calculation time required in the case of high-resolution images. The proposed algorithm was based on the initial assumption that a legend would be placed on the left-hand side of the image, giving the ρ ranges allowing determination of the image colours. The pattern of colour areas is represented in Figure 5.

The algorithm is equipped with Optical Character Recognition (OCR) feature to recognise the numerical values of the ranges in the Legend portion and thus generate a report. AI based Tesseract engine [29], one of the most accurate character recognition engines, was used for this purpose.

In the first phase the Legend portion was analysed to determine the colour values present in the simulation output image (Fig. 3 (2)). Black and white colours were ignored in the colour analysis of the Legend portion. Next the simulation output portion of the image was converted to HSF colour space and numerical ranges (upper and lower) were determined for each determined colour of the Legend portion of the image. The numerical ranges were calculated as follows:

$$\text{lower} = [\text{clip}(H - 1, 0, 180), 10, 10] \tag{1}$$

$$\text{upper} = [\text{clip}(H + 1, 0, 180), S, V] \tag{2}$$

where: H – value of HSV colour space hue;
S – value of HSV saturation;
V – HSVcolour space value.

For each colour range a bitmask was created of the same resolution as the simulation output image. Next the bitmask matrix was multiplied with the simulation output image using bitwise AND operation. This operation yielded an output image composed of white and black pixels. In each bitmask white pixels represented pixels from the respective colour ranges. White pixels were summed up for each range. The share of the
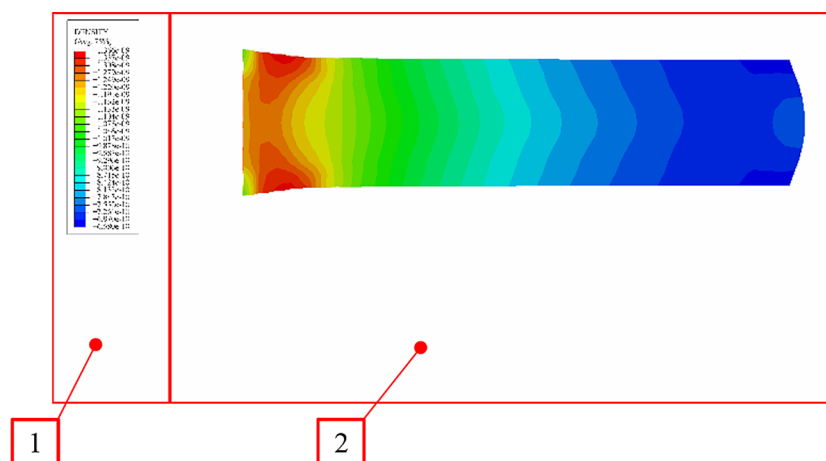

Fig. 5. Pattern of colour areas representing the output of numerical simulation, 1 – legend portion; 2 – simulation output portion with the results represented by colour pixels
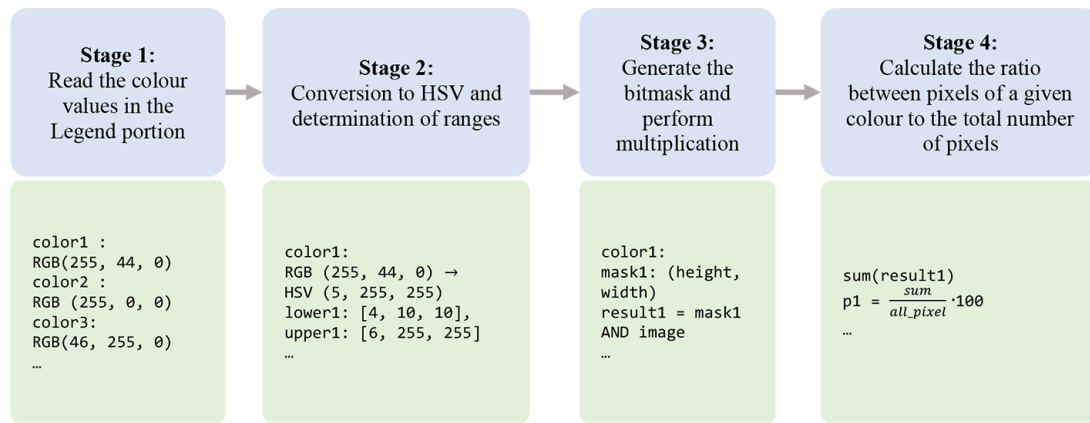
Stage 1: Read the colour values in the Legend portion	Stage 2: Conversion to HSV and determination of ranges	Stage 3: Generate the bitmask and perform multiplication	Stage 4: Calculate the ratio between pixels of a given colour to the total number of pixels
color1 : RGB(255, 44, 0) color2 : RGB (255, 0, 0) color3: RGB(46, 255, 0) …	color1: RGB (255, 44, 0) → HSV (5, 255, 255) lower1: [4, 10, 10], upper1: [6, 255, 255] …	color1: mask1: (height, width) result1 = mask1 AND image …	sum(result1) $p1 = \frac{sum}{all\_pixel} \cdot 100$ …

Fig. 6. Algorithm to determine the number of pixels of the same colour. Step 1: Read the colour values in the Legend portion; Step 2: Conversion to HSV and determination of ranges; Step 3: Generate the bitmask and perform multiplication; Step 4: Calculate the ratio between pixels of a given colour to the total number of pixels

respective colours in the entire simulation output image was the product of sum of white pixels for a given colour divided by the sum of all pixels for a given simulation output image. This algorithm is summed up in the diagram in Figure 6.

The program allows automatic analysis of the dry ice extrusion process simulation output through analysing the images stored on the hard drive at a specific file path. The output analysis is generated as a *PNG* and *CSV* file report. The program code was written in Python.

Numerical analysis

The numerical model was developed in ABAQUS and the simulations were carried out in Explicit module. The process of extrusion through a was simulated using a die model such as the single-cavity conical-cylindrical die shown in Figure 7.

This model is composed of three parts: single-cavity die (1), ram (2) and extruded material (3). For the purposes of this analysis the single-cavity die (1) was integrated with the compression cavity to allow simplification of the geometrical model, yielding a more uniform distribution of the finite element grid. Inside the top part of the die there moves the ram (2), sliding without friction. The extruded material (3) – dry ice – was modelled as an axisymmetric solid having the outside shape and dimensions defined by the shape of the hole in the upper part of the die. Two reference points have been defined, that play an important role in the analysis:

- reference point of the integrated single-cavity die (4), coupled to the solid element representing the die (1), located in the die base plane and in its axis of symmetry,

- ram reference point (5), coupled to the ram solid element (2) and located on its upper side surface and on he axis of symmetry.

These points are used to set the ram and die initial/ boundary conditions. The following assumptions were made in the single-cavity extrusion process simulation:
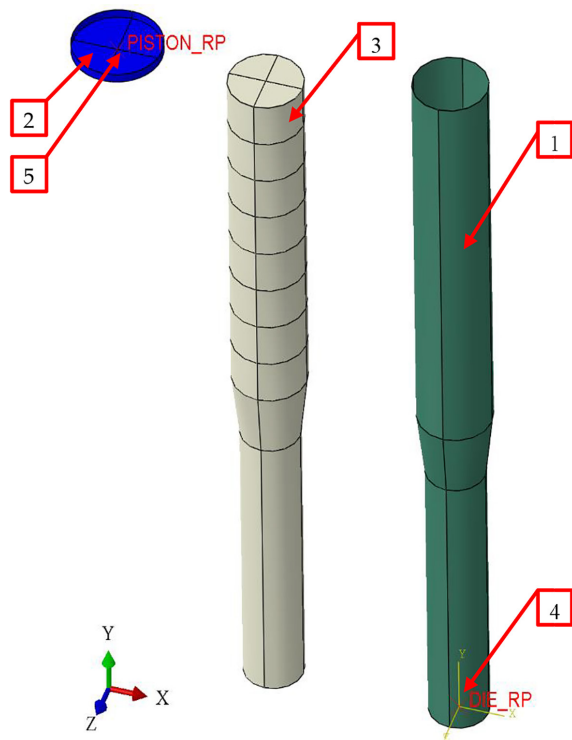

Fig. 7. An example of geometrical model of the components before their assembly, implemented in numerical calculations based on the process of extrusion in a single-cavity extrusion die featuring a conical convergent section: (1) integrated single-cavity die, (2) ram, (3) extruded material (dry ice), (4) reference point of the integrated single-cavity die, (5) ram reference point

1. General:
a) The simulation was carried out in ABAQUS/ Explicit.
b) The analysis duration was 32 sec.
c) The time step was 0.0001 sec., defined by the Mass Scaling parameter.

2. Die model parameters:
a) The die was modelled as analytical rigid shell.
b) The die was coupled with a cylindrical compression cavity of a constant inside diameter of $D = 20$ mm.
c) The model was discretized by R3D4 with circularly symmetric distribution about the Y axis of the model (Fig. 8). Approximate distance between nodes equal to 2 mm.
d) Total number of nodes was equal to 2408 and the total number of elements was equal 2380.
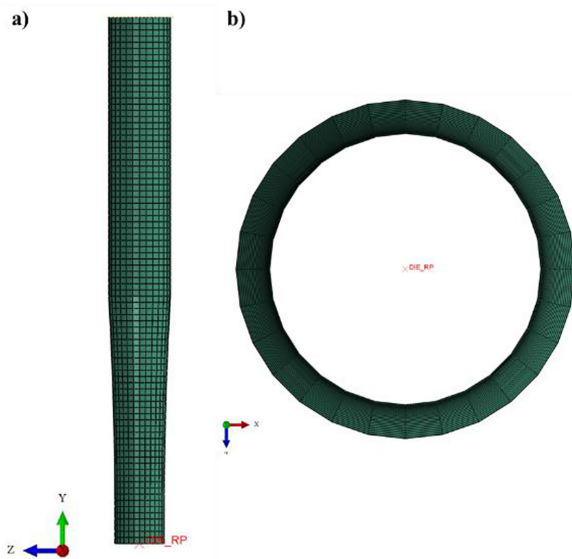
Fig. 8. Example of finite elements distribution for a single-cavity die: (a) in longitudinal section, (b) in cross-section

3. Ram model parameters:
a) The same as the die, the ram was modelled as analytical rigid shell.
b) It had inside diameter $D' = 24$ mm to avoid conflicts when the extruded material would go beyond the ram surfaces.
c) The finite element parameters were like those used in die discretization and an example of finite element distribution is shown in Figure 9.
d) Ram and die had no defined contact, thus leaving out any motion resistance of these models in relation to each other.

4. Parameters of the extruded material model:
a) The extruded material model was defined as a deformable body.
b) The model's shape corresponded to the shape of the die cylindrical section.
c) The same element as in the previous models was used for discretization, i.e. R3D4 with an approximate distance between nodes equal to 2 mm.
d) Total number of nodes was equal to 7371 and the total number of elements was equal 6080.
e) The model body was defined using two domains. The first of them, initially located inside the 20 mm dia. cylindrical section was described by means of Drucker-Prager/Cap model, using the parameters obtained from the literature [22]. On the extruded material section inside the die convergent section, elastic-plastic material model was applied with the mechanical parameters consistent with the reported simulations [24].

Similar assumptions related to the description of the respective model elements were applied for the multiple-cavity die extrusion process simulation. The main differences between the assumptions were:

1. General:
a) The analysis duration was 13 sec.
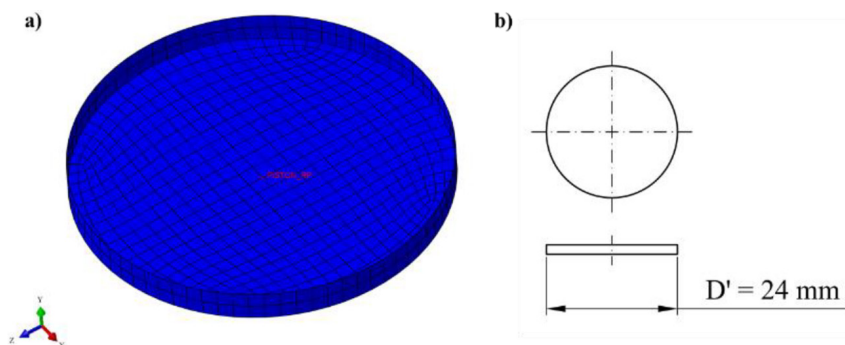b) The Mass Scaling value was 0.001 sec.

Fig. 9. Example of finite elements distribution for the compressing ram: a) overview, b) geometric features

2. Parameters of the extruded material model
a) The material domain inside the die cavities was modelled as elastic-plastic body
b) The material domain inside the cylindrical cavity before the multi-cavity die was discretized with the Smoothed Particle Hydrodynamics (SPH) method to avoid conflicts during extrusion of the material to the respective die cavities.

The construction of the respective models is illustrated schematically in Figure 10 and the SPH discretized material model is shown in Figure 11.

RESULTS AND DISCUSSIONS

The outputs of DI extrusion simulation using single-cavity dies are illustrated below. Fig. 12 shows the simulation output obtained for CS convergent section dies, Figure 16 for WP convergent section dies, and Figure 20 for WKWP. Below the drawings there are bar graphs giving the percentages of the respective ρ ranges.

The values were compared showing differences between the distributions of values on the numerical simulation images and those
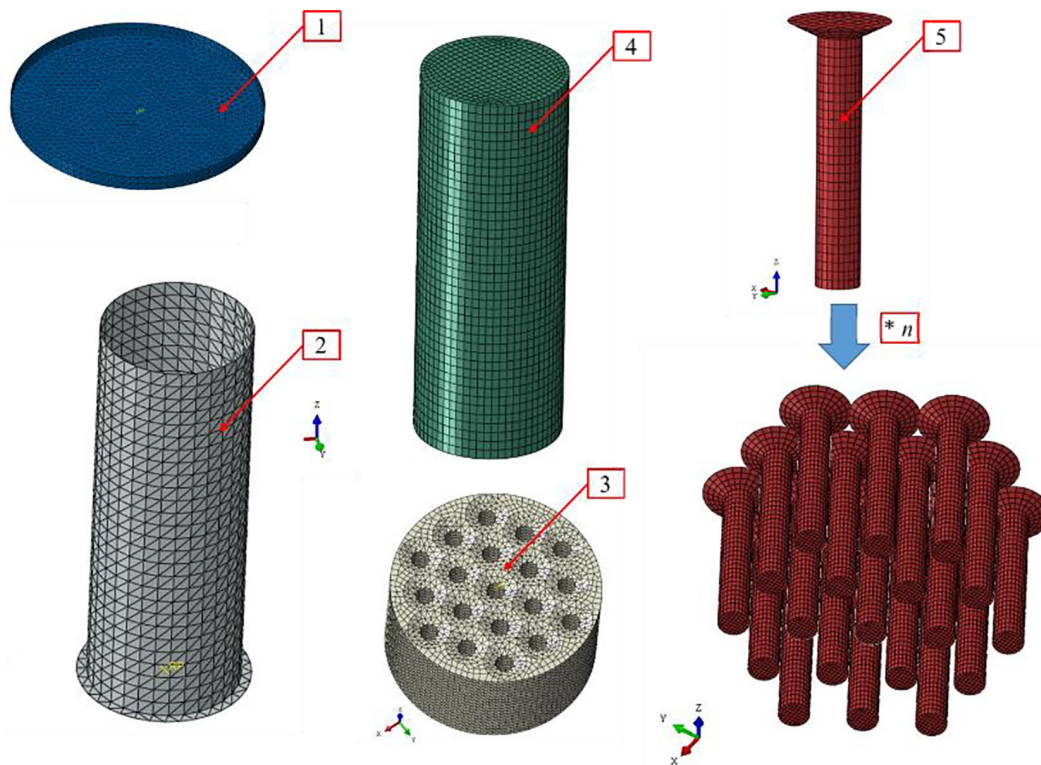
Fig. 10. A discretized model implemented in numerical calculations based on the process of extrusion in a multiple-cavity extrusion die featuring a conical compression cavity before assembly: 1 – ram, 2 – feed sleeve, 3 – multi-cavity die, 4 – loose dry ice, 5 – dry ice after compression
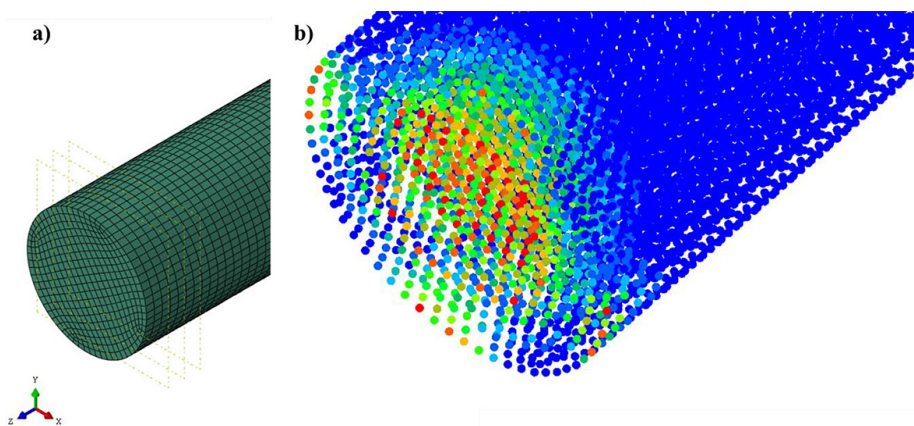
Fig. 11. Example of finite element distribution for the loose dry ice domain before extrusion (a) and example of SPH distribution during reading the output of the analysis (b)
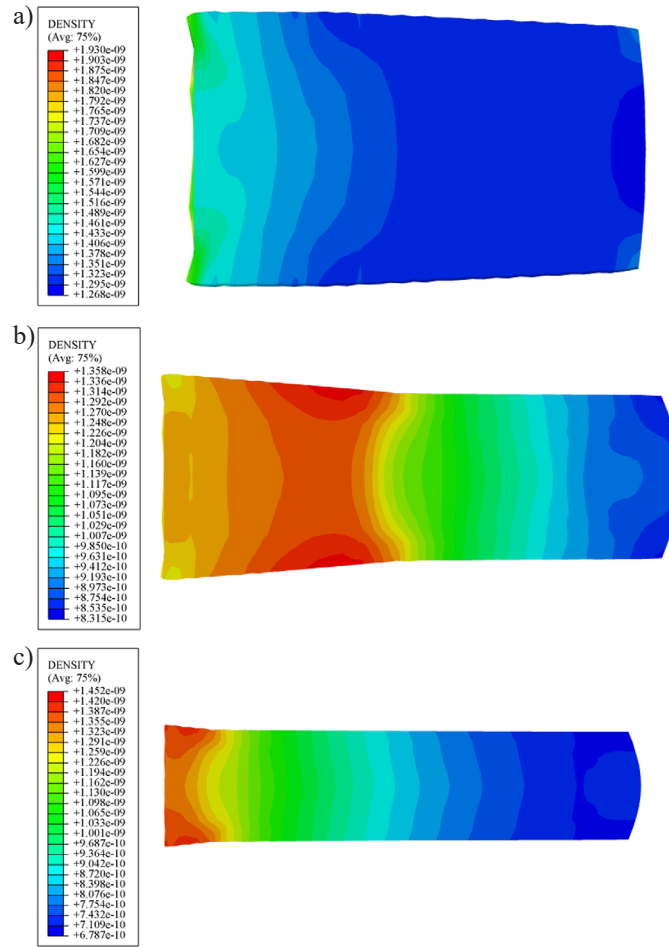
Fig. 12. Output of DI extrusion simulation using single-cavity dies featuring a conical convergent section (CS): (a) α = 3°; (b) α = 5°; (c) α = 7°
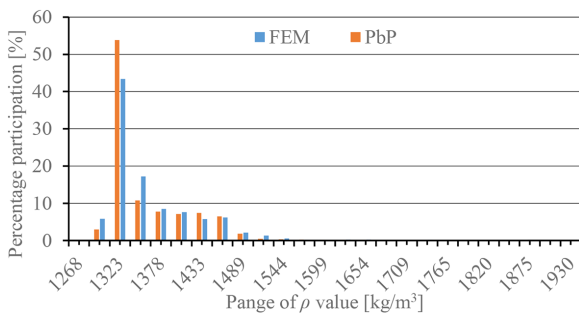

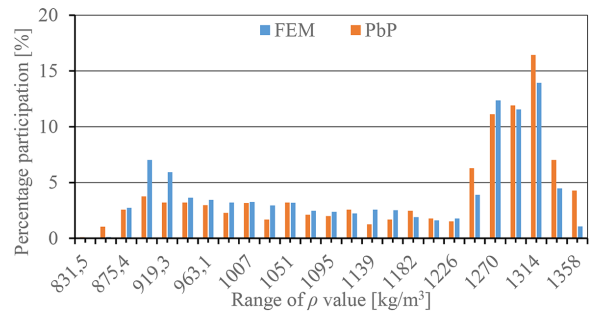**Fig. 13.** Bar chart of the percentage share of ρ values for CS die simulation of α = 3°

Fig. 14. Bar chart of the percentage share of ρ values for CS die simulation of α = 5°

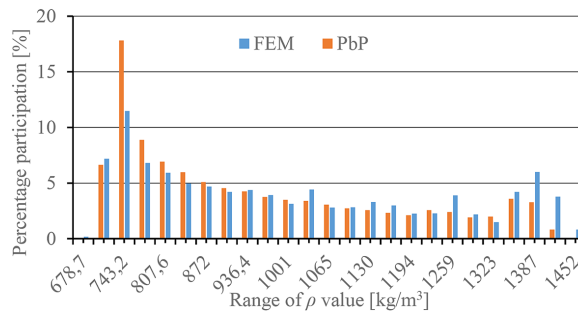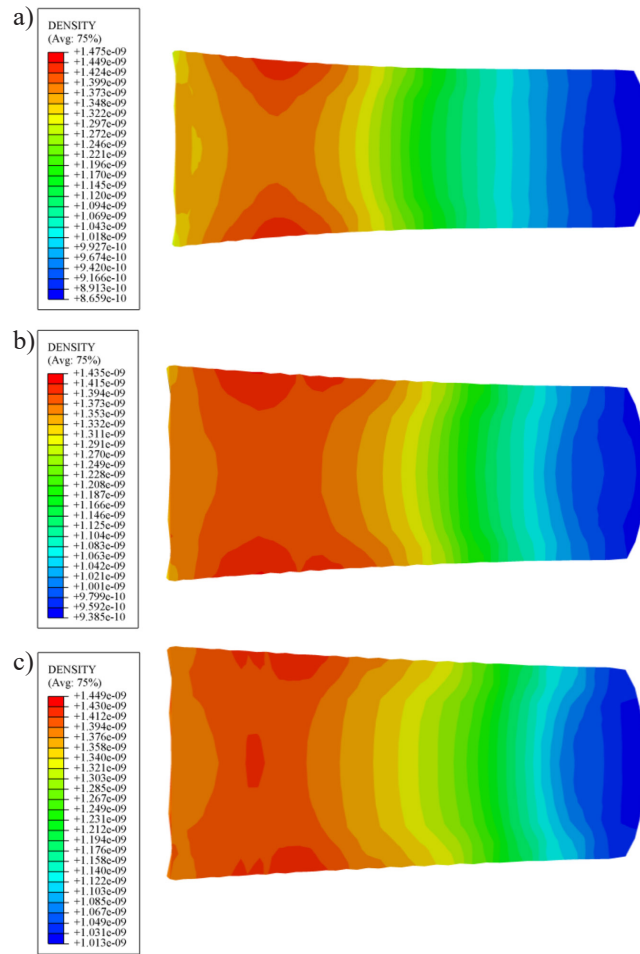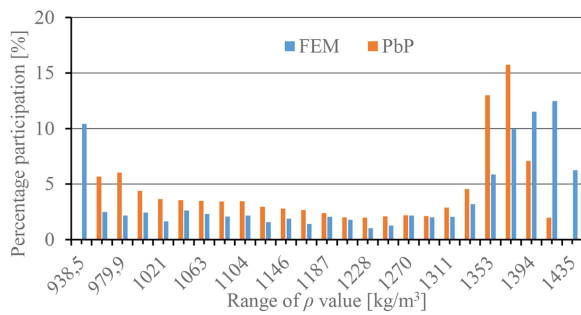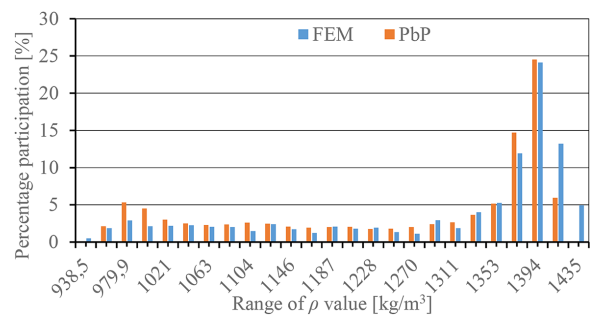**Fig. 15.** Bar chart of the percentage share of ρ values for CS die simulation of α = 7°

Fig. 16. Output of DI extrusion simulation using single-cavity dies featuring a convex convergent section (WP): (a) h = 30; (b) h = 40; (c) h = 50

Fig. 17. Bar chart of the percentage share of ρ values for WP die simulation of h = 30

Fig. 18. Bar chart of the percentage share of ρ values for WP die simulation of h = 40
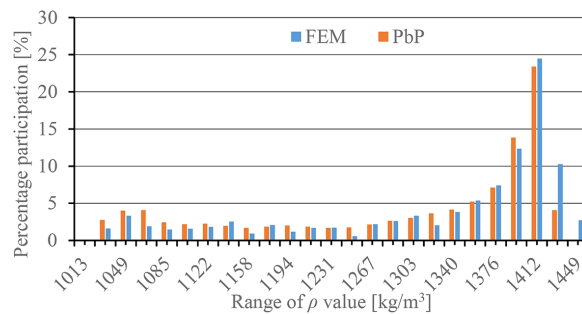

Fig. 19. Bar chart of the percentage share of ρ values for WP die simulation of h = 50
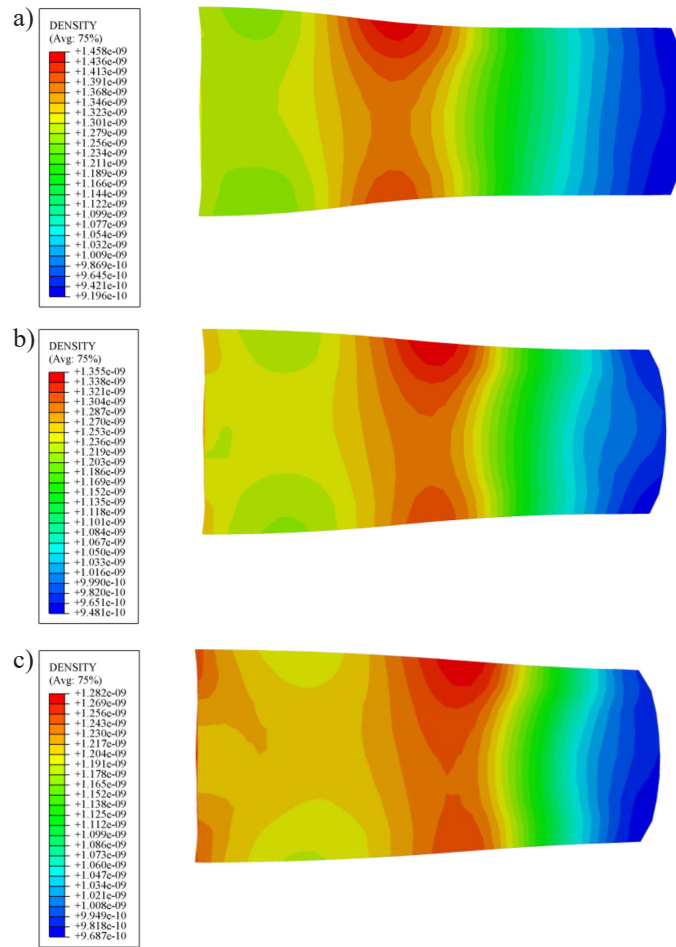
Fig. 20. Output of DI extrusion simulation using single-cavity dies featuring a convex convergent section (WKWP): (a) h = 30; (b) h = 40; (c) h = 50
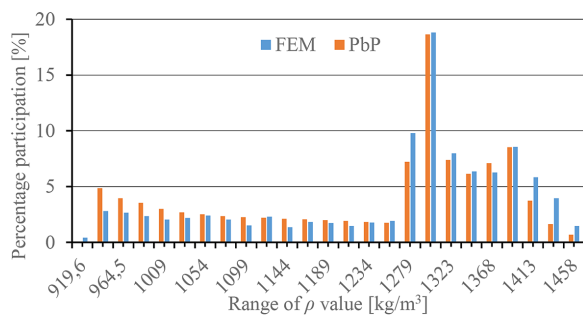

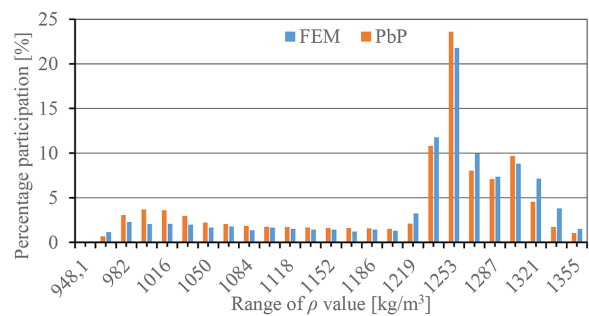**Fig. 21.** Bar chart of the percentage share of ρ values for WKWP die simulation of h = 30

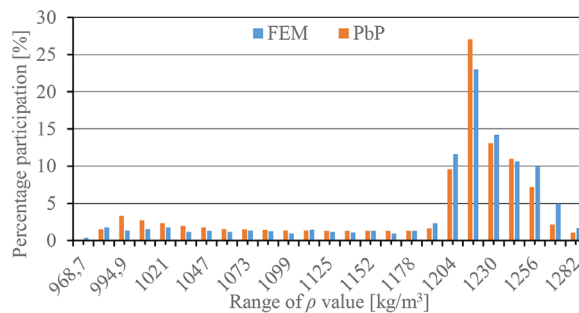**Fig. 22.** Bar chart of the percentage share of ρ values for WKWP die simulation of h = 40

Fig. 23. Bar chart of the percentage share of ρ values for WKWP die simulation of h = 50
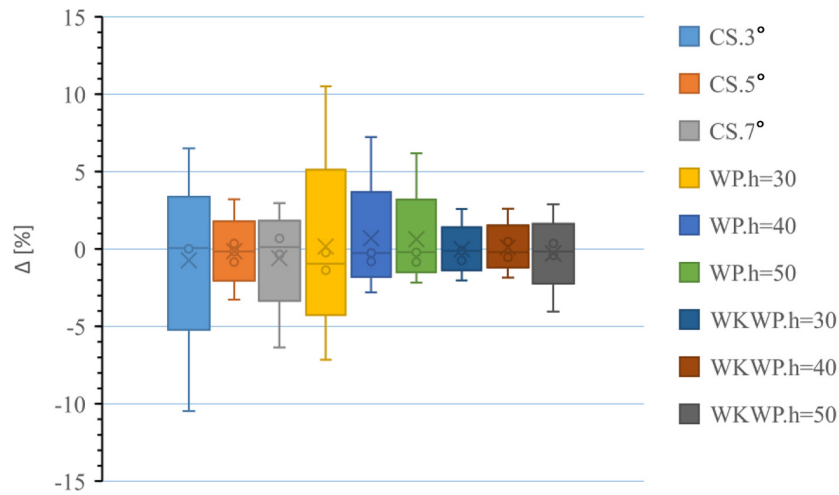
Fig. 24. Box plot of the general statistical data concerning differences between populations of the percentage share of ρ ranges
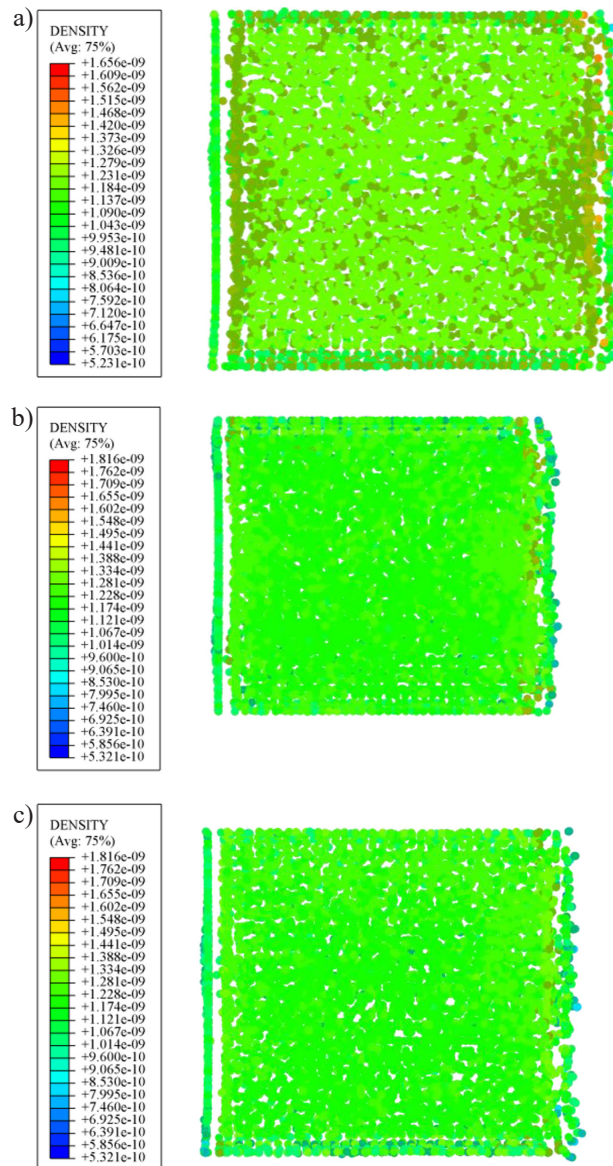

Fig. 25. DI extrusion process simulation output using multi-cavity die (MCD) for three cutting planes tilted at different angles: (a) S-0°; (b) S-45°; (c) S-90°

contained in the database. These differences concern in particular the percentage share in the extreme ranges.

For comparison of the respective single-cavity dies, the percentage share differences were determined for each range. They are illustrated in the following box and whisker plots representing the main statistical parameters.

For the results obtained in the simulation using CS of $\alpha = 3°$, WP of $h = 30$ and WP of $h = 50$ dies the maximum difference of values exceeded the 7% threshold. The percentage difference median, in turn, did not exceed the 1% threshold.

The differences between the database and the values obtained through the image processing are caused, inter alia, by the fact that the images

illustrate the values at the numerical grid nodes located in the cutting plane passing through the extruded DI model. Notwithstanding the use of circularly symmetric models, there have still remained grid elements for which ρ exceeded the extreme ranges. Therefore, the number of left out elements for the adopted ρ ranges was checked giving for WP of $h = 40$ die 351 No. per the total number of 3040 values contained in the process simulation database. In the case of WP 3 No. extreme values of the left-out elements were noted, which justifies the Fig. 24 results.

The next step of the analysis concerned the density field distribution in multiple-cavity die extrusion process. For this purpose, numerical simulation output images were generated on three planes tilted at different angles, i.e. S-0°, S-45° and S-90°. The output is illustrated in Fig. 25 and in the bar charts in Fig. 26-28, same as for single-cavity dies.

The bar chart comparing the results obtained in S-0° features the consistency of results same as for the charts of circularly symmetric models. Conversely, in S-45° and S-90° planes there is a clearly discernible difference in the percentage share of the respective ρ ranges between the numerical analysis data base and the data represented on the plane. Therefore, considering these clearly discernible differences box-plot was not generated.

In line with the initial assumption, the presented results show that visual representation of the outputs of numerical simulations using circularly-asymmetric models may feature high non-consistency with the computed values database. This being so, we would not recommend the use of the proposed method for determining the percentage share of different colours on the numerical simulation output images.
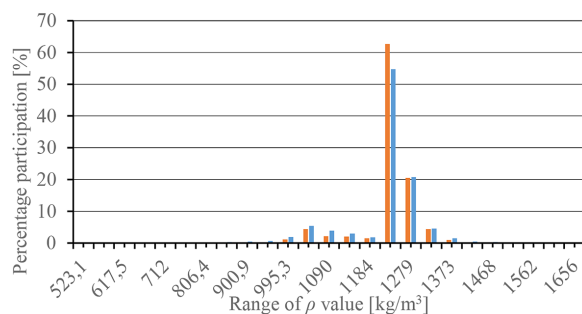

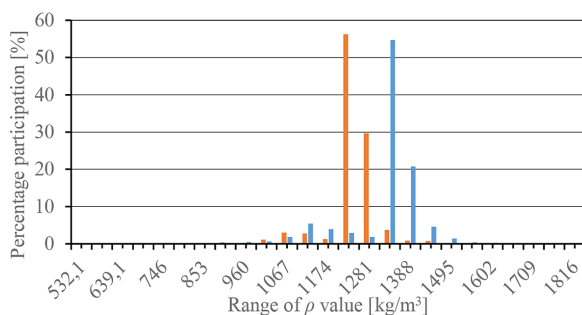**Fig. 26.** Bar chart of the percentage share of ρ values for WKWP die simulation in S-0° cutting plane

Fig. 27. Bar chart of the percentage share of ρ values for WKWP die simulation in S-45° cutting plane
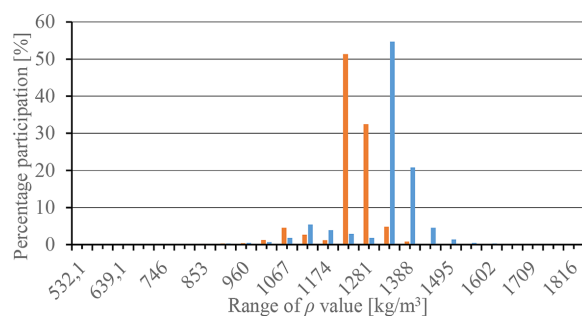

Fig. 28. Bar chart of the percentage share of ρ values for WKWP die simulation in S-90° cutting plane

CONCLUSIONS

The study result presented in this article allow determination of the performance of the analysed algorithm for analysing the distribution of fields in the numerical analysis output images. The difference between the values obtained with the method under analysis reached up to 7%, noting that in two out of three elements of the population 11.5% of the data were not represented in the model cross-section. The authors are of the opinion that the magnitude of difference between the database values and the values obtained from

image processing has no significant bearing on the simulation output interpretation in the case of simulations using circularly symmetrical models. The tool allows comparison of the respective values when data base values are not available in the literature, as it is often the case.

However, in the case of models featuring high variability of values depending on the cutting plane location, i.e. the plane with the graphically represented value in question, the accuracy of the proposed method is low.

Still, we believe that while the proposed method may be used to fill the gap in the numerical output analysis area there is still a need for development of software for analysing the output of simulation studies.

Acknowlegments

REFERENCES

1. Gawrońska, E., Dyja, R., Zych, M., Domek, G. Selection of the Heat Transfer Coefficient Using Swarming Algorithms. Acta Mech. Et Autom. 2022; 16(4): 325–339. https://doi.org/10.2478/ama-2022-0039

2. Gierz, Ł., Warguła, Ł., Kukla, M., Koszela, K., Zawiachel, T. Computer Aided Modeling of Wood Chips Transport by Means of a Belt Conveyor with Use of Discrete Element Method. Appl. Sci. 2020; 10(24). https://doi.org/10.3390/app10249091

3. Markowski, J., Pielecha, I. The potential of fuel cells as a drive source of maritime transport, IOP Conference Series: Earth and Environmental Science. 2019; 214. DOI: http://dx.doi.org/10.1088/1755-1315/214/1/012019

4. Wilczyński, D., Talaśka, K., Wojtokwiak, D., Wałęsa, K., Wojciechowski S. Selection of the Electric Drive for the Wood Waste Compacting Unit. Energies. 2022; 15(20). DOI: http://dx.doi.org/10.3390/en15207488

5. Omer, O., Alireza K. Alternative Energy in Power Electronics: Chapter 2 Energy in Power Electronics, Butterworth-Heinemann. 2015; 81–154. https://doi.org/10.1016/B978-0-12-416714-8.00002-0

6. Jesionek, K., Wieczorkiewicz, G., Rychlik M., Riczak, R., Markowski, J., Nowacki M., Olejniczak, D., Wasiński K. Problems of Plastic Recycling in the Aspect of the Applications of Energy Methods. Journal of Engineering Science and Technology Review. 2020; 176–279.

7. Tahmasebi, M.M., Banihashemi, S., Hassanabadi, M.S. Assesment of the Variation Impacts og Windwos on Energy Consumption and Carbon Footprint, Procedua Engineering. 2011; 21: 820–828. https://doi.org/10.1016/j.proeng.2011.11.2083

8. Bydełek, A., Berdychowski, M., Talaśka, K. Modeling of Material Characteristics of Conventional Synthetic Fabrics, Autex Research Journal. 2022; 2. https://doi.org/10.2478/aut-2022-0002

9. Raza, S., Ahmad, J. Composting process: a review. International Journal of Biological Research. 2016; 4(2): 102–104. https://doi.org/10.14419/ijbr.v4i2.6354

10. Lohri, C., Rajabu, H., Sweeney, D., Zurbrügg, C. Char fuel production in developing countries – A review of urban biowaste carbonization. Renewable and Sustainable Energy Reviews. 2016; 59: 1514–1530. https://doi.org/10.1016/j.rser.2016.01.088

11. Wilczyński, D., Berdychowski, M., Talaśka, K., Wojtkowiak, D. Experimental and numerical analysis of the effect of compaction conditions on briquette properties. Fuel. 2021; 288: 119613. https://doi.org/10.1016/j.fuel.2020.119613

12. Uhryński, A., Bembenek, M. The Thermographic Analysis of the Agglomeration Process in the Roller Press of Pillow-Shaped Briquettes. Materials. 2022; 15(8): 2870. https://doi.org/10.3390/ma15082870

13. Mani, S., Tabil, L., Sakhansanj, S. Specific energy requirement for compacting corn stover. Bioresource Technology. 2006; 97(12): 1420–1426. https://doi.org/10.1016/j.biortech.2005.06.019

14. Pasciucco, F., Francini, G., Pecorini, I., Baccioli A., Lombardi, L., Ferrari, L. Valorization of biogas from the anaerobic co-treatment of sewage sludge and organic waste: Life cycle assessment and life cycle costing of different recovery strategies. Journal of Cleaner Production. 2023; 401: 136762. https://doi.org/10.1016/j.jclepro.2023.136762

15. Bicer, Y., Dincer, I., Vezina, G., Raso, F. Impact Assessment and Environmental Evaluation of Various Ammonia Production Processes, Environmental Management. 2017; 59: 842–855. https://doi.org/10.1007/s00267-017-0831-6

16. Dzido, A., Krawczyk, P., Badyda, K., Chondrokostas, P. Operational characteristics impact on the performance of dry-ice blasting nozzle. Energy. 2021; 214: 118847. https://doi.org/10.1016/j.energy.2020.118847

17. Witte, A.K., Bobal, M., David, R., Blättler, B., Schoder, D., Rossmanith, P. Investigation of the potential of dry ice blasting for cleaning and disinfection in the food production environment. LWT. 2017; 75: 735–741. https://doi.org/10.1016/j.lwt.2016.10.024

18. Spur, G., Uhlman, E., Elbing, F. Dry-ice blasting for cleaning: process, optimization and application, Wear. 1999; 233–235: 402–411. https://doi.org/10.1016/S0043-1648(99)00204-5

19. Liu, Y.H., Matsusaka, S.L. Formation of Dry Ice Particles and Their Application to Surface Cleaning. Earozoru Kenkyu. 2013; 28: 155–162. https://doi.org/10.11203/jar.28.155

20. Górecki, J., Talaśka, K., Wałęsa, K., Wilczyński, D., Wojtkowiak, D. Mathematical model describing the influence of geometrical characteristics of multichannel dies on the limit force of dry ice extrusion process. Materials. 2020; 13(15): 3317. https://doi.org/10.3390/ma13153317

21. Górecki, J., Wałęsa, K., Biszczanik, A. Determination of the density of solid carbon dioxide using the hydrostatic method. AIP Conference Proceedings, 2023.

22. Berdychowski, M., Górecki, J., Biszczanik, A., Wałęsa, K. Numerical Simulation of Dry Ice Compaction Process: Comparison of Drucker-Prager/Cap and Cam Clay Models with Experimental Results. Materials. 2022; 15: 5771. https://doi.org/. https://doi.org/10.3390/ma15165771

23. Górecki, J., Łykowski W. Influence of Die Land Length on the Maximum Extrusion Force and Dry Ice Pellets Density in Ram Extrusion Process. Materials. 2023; 16(12): 4281. https://doi.org/10.3390/ma16124281

24. Wałęsa, K., Górecki, J., Berdychowski, M., Biszczanik, A., Wojtkowiak, D. Modelling of the Process of Extrusion of Dry Ice through a Single-Hole Die Using the Smoothed Particle Hydrodynamics (SPH) Method. Materials. 2022; 15(22). http://dx.doi.org/10.3390/ma15228242

25. Berdychowski, M., Górecki, J., Wałęsa, K. Numerical Simulation of Dry Ice Compaction Process: Comparison of the Mohr–Coulomb Model with the Experimental Results. Materials. 2022; 15(22): 7932. https://doi.org/10.3390/ma15227932

26. Tiernan, P., Hillery, M.T., Draganescu, B., Gheorghe M. Modelling of cold extrusion with experimental verification. Journal of Materials Processing Technology. 2005; 168(2): 360–366. https://doi.org/10.1016/j.jmatprotec.2005.02.249

27. Biszczanik, A., Wojtkowiak, D., Wałęsa, K. Influence of the geometric characteristics of convergent extrusion channel of die on the maximum value of compaction stress of dry ice and on the quality of the obtained pellets. AIP Conference Proceedings, 2023, (submitted; accepted; in press).

28. Georgieva, L., Dimitrova, T., Angelov, N. RGB and HSV colour models in colour identification of digital traumas images, International conferences on computer systems and technologies, 2005, 12(1).

29. Hema, D.M., Kannan, D.S. Interactive color image segmentation using HSV color space. Science and Technology Journal. 2029; 7(1). http://doi.org/10.22232/stj.2019.07.01.05

30. Smith, R. An Overview of the Tesseract OCR Engine. Ninth International Conference on Document Analysis and Recognition. 2007; 2: 629–633. DOI: https://doi.org/10.1109/ICDAR.2007.4376991